The Astrophysical Journal, 697:999–1009, 2009 June 1 doi:10.1088/0004-637X/697/2/999

HARD X-RAY EMISSION IN KINKING FILAMENTS

Rui Liu[1], and David Alexander
Department of Physics and Astronomy, Rice University, Houston, TX 77005, USA; rui.liu@njit.edu.
Received 2008 December 30; accepted 2009 March 20; published 2009 May 6

ABSTRACT

We present an observational study on the impact of the dynamic evolution of kinking filaments on the production of hard X-ray (HXR) emission. The investigation of two kinking-filament events in this paper, occurring on 2003 June 12 and 2004 November 10, respectively, combined with our earlier study on the failed filament eruption of 2002 May 27, suggests that two distinct processes take place during the kink evolution, leading to HXR emission with different morphological connections to the overall magnetic configuration. The first phase of the evolution (Phase I) is characterized by compact HXR footpoint sources at the endpoints of the filament, and the second phase (Phase II) by a ribbon-like footpoint emission extending along the endpoints of the filament. The HXR emission in both the 2002 May 27 and 2004 November 10 events shows a transition from Phase I to Phase II. In the 2002 May 27 event, coronal emission was observed to be associated with EUV brightening sheaths aligned along two filament legs in Phase I, while in Phase II, it was located near the projected crossing point of the kink. The coronal emission in the 2004 November 10 event does not exhibit a clear morphological transition as in the 2002 May 27 event, probably due to the filament's relatively small size. The 2003 June 12 event mostly features a Phase I emission, with a compact footpoint emission located at one end of the filament, and an elongated coronal source oriented along the same filament leg. We propose the following scenarios to explain the different flare morphology: magnetic reconnection in Phase I occurs as a result of the interactions of the two writhing filament legs; reconnection in Phase II occurs at an X-type magnetic topology beneath the filament arch when the filament ascends and expands.

Key words: Sun: filaments – Sun: flares – Sun: X-rays, gamma rays

Online-only material: color figures, avi animation

1. INTRODUCTION

Eruptive filaments which display a warped axis are generally regarded as the "fingerprint" of the MHD helical kink instability (e.g., Rust & LaBonte 2005). A magnetic flux rope becomes kink-unstable if the twist of the field, Tw, a measure of the number of windings of field lines about the rope axis, exceeds a critical value of order 2π (e.g., Hood & Priest 1979). This results in a transfer from the twist to the writhe of the field, Wr, a measure of the twist of the rope axis itself, as the magnetic helicity, $H = \Phi^2(\mathrm{Tw} + \mathrm{Wr})$, is essentially conserved in the highly conducting corona (Berger 1984), where Φ is the magnetic flux within the rope. Recent observations of kinking motions in a number of filament eruptions with a range of different natures, including full filament eruption (Williams et al. 2005), partial cavity eruption (Liu et al. 2007), partial filament eruption (Liu et al. 2008), and failed filament eruption (Ji et al. 2003; Alexander et al. 2006), suggest the kink instability as an important process in the interactions of the filament with its magnetic environment.

The kink instability has long been investigated as a possible triggering mechanism for solar eruptive phenomena (see the review by Hood 1992), especially in flux rope models. While the straight flux tube configuration has been studied in depth (e.g., Baty & Heyvaerts 1996; Lionello et al. 1998; Baty 2000; Gerrard et al. 2001; Gerrard & Hood 2003), the effects of curvature on the flux tube have been explored more recently. Numerical simulations have shown how the current sheets form (e.g., Török et al. 2004; Gibson et al. 2004), how the flux rope responds to twist being injected through the footpoints (e.g., van Hoven et al. 1995; Amari et al. 1996; Amari & Luciani 1999; Klimchuk et al. 2000; Török & Kliem 2003; Gerrard et al. 2004; Aulanier et al. 2005), and how the kink-unstable flux rope erupts through the overlying arcades (e.g., Török & Kliem 2005; Fan 2005).

Simulations by Török and Kliem (hereafter T&K; Török et al. 2004; Kliem et al. 2004; Török & Kliem 2005) show the formation of a helical current sheet enwrapping a flux rope and a vertical current sheet underneath the flux rope during its kink evolution. Alternatively, simulations by Fan and Gibson (hereafter F&G; Fan & Gibson 2003, 2004; Gibson et al. 2004; Fan 2005; Gibson & Fan 2006) show that as a flux rope kinks and expands upward, a vertical S-shaped current sheet is formed within the flux rope. The current sheets forming during the kink evolution have been used to explain the bright sigmoidal structures seen in soft X-ray or EUV observations (see reviews by Gibson et al. 2006; Green et al. 2007). In the failed filament eruption on 2005 May 27, EUV brightening sheaths were observed to be oriented along the legs of the kinking filament (Ji et al. 2003), and a hard X-ray (HXR) coronal source (12–25 keV) is observed to be located close to the projected crossing point of the kink (Alexander et al. 2006). In the partial cavity eruption on 2003 October 31, an HXR coronal source (12–25 keV) also appeared below the apex of the kinking filament, as seen from the side, at about the filament's half-height (Liu et al. 2007). However, the association of these emission features with the current sheets in either T&K or F&G simulations remains unclear.

Both T&K and F&G are variants of a three-dimensional analytical model constructed by Titov & Démoulin (1999) (hereafter T&D). The field configuration of T&D excludes the

[1] Current address: Space Weather Research Laboratory, Center for Solar-Terrestrial Research, NJIT, Newark, NJ 07102, USA.

existence of any null point, but the presence of *bald patches* (BPs; Seehafer 1986; Titov et al. 1993) makes it relevant to solar flares. BPs are the segments of the photospheric inversion line where the coronal field lines touch the photosphere tangentially. The field lines starting at a BP form a *bald-patch-associated separatrix surface* (BPSS; Titov & Démoulin 1999; Low & Berger 2003), along which sigmoid current sheets could form as a result of dynamic perturbations of the flux rope lying above and within this BPSS. When the flux rope only partly "emerges" above the photosphere, there is a single, continuous BP of dipped field grazing the central portion of the neutral line. As the flux tube continues to emerge and grow, the BP bifurcates, or disappears altogether, giving birth to a *hyperbolic flux tube* (HFT; Titov et al. 2002) below the flux rope, where a transition to a topologically simple arcade-like configuration occurs (Titov & Démoulin 1999; Roussev et al. 2003). The HFT is a generalized separator field line, which could be regarded as a three-dimensional counterpart of the X-type magnetic topology in the standard flare model. It may be current free initially, but can pinch into a vertical layer with exponentially rising current density due to external perturbations (Titov et al. 2003).

Thus, if a flux rope lies high enough in the atmosphere, a HFT will be present below the flux rope, and the reconnection in the vicinity of the HFT would result in the flux rope being completely expelled, leaving behind cusped, post-flare fields, which is the case in the T&K simulations using the T&D model with no BP as the starting point. On the other hand, in the F&G simulations, the flux rope is driven from below the photosphere slowly into the corona previously occupied by a potential arcade. At the onset of the kink instability, the two legs of the flux rope are squeezed together and the BPSS is dynamically forced, where sigmoid field lines reconnect, thereby breaking the rope in two and resulting in a partial eruption with a less sigmoid-shaped and more cusp-shaped BPSS left behind.

In this paper, we utilize spatially resolved HXR data from *RHESSI* and high-resolution EUV/UV data from *TRACE* to explore the locations of possible reconnection sites and analyze how this relates to current sheets formed during the kink evolution as demonstrated in numerical simulations. First we revisit the kinking filament on 2002 May 27, which is associated with an M-class flare, then we investigate the HXR emission in a peculiar "twin" kinking-filament event taking place on 2003 June 12, associated with an M-class flare, and finally a kinking filament on 2004 November 10, associated with an X-class flare. Due to the relative rarity of kinking filaments, only the three events aforementioned have been brought to our awareness so far, which both show a clear kinked structure and have good coverage in the relevant data sets. Observations and data analysis are presented in Section 2, and the results are discussed in Section 3.

2. OBSERVATIONS AND DATA ANALYSIS

2.1. Instruments and Co-alignment

All three events studied here are well observed by *RHESSI* and *TRACE*. *RHESSI* is a rotating modulation collimator from which HXR images can be reconstructed via a detailed analysis of the received modulation patterns (Hurford et al. 2002). While a number of image reconstruction techniques are available, we choose to work with the most computationally expensive one, the Pixon reconstruction method (Metcalf et al. 1996; Alexander & Metcalf 1997), which is superior in photometry, positional accuracy, and weak-source detection, while mitigating the problems of correlated residuals and spurious sources that often plague the Fourier deconvolution and maximum entropy approaches (Aschwanden et al. 2004). Detectors 3–8 are used in this study unless specified differently, and the spatial resolution is largely dictated by detector 3 which has the finest FWHM angular resolution ($\sim 7''$) among the detectors being used.

The *TRACE* telescope has a field of view (FOV) of $8'.5 \times 8'.5$ and a spatial resolution of $1''$ (0.5 arcsec pixels) with a typical time cadence of less than 10 s for the UV continuum band in the flare mode, and less than 1 minute for EUV bands. An unknown and time-varying offset in the TRACE pointing is caused by flexures of the instrument metering tube that supports the telescope, making the determination of its absolute pointing difficult. This can result in errors of more than $10''$ in the *TRACE* pointing knowledge (e.g., Alexander & Coyner 2006). Thus, care must be taken when comparing *TRACE* observations with other instruments.

In this study, three different approaches are taken to correct the *TRACE* pointing. In the 2003 June 12 event, we cross-correlate an image obtained in the *TRACE* WL channel (2003 June 12 01:06:08 UT) with a Michelson Doppler Imager (MDI) continuum image (2003 June 11 23:59:32 UT), using the routine developed by T. Metcalf (Metcalf et al. 2003), trace_mdi_align, in the Solar SoftWare (SSW), and find that the *TRACE* pointing should be corrected by $-3''.4$ in the *X*-direction and $-4''.2$ in the *Y*-direction. Alternatively, following Aulanier et al. (2000), we overlay one *TRACE* 1700 Å image obtained prior to the flare (2003 June 12 01:00:03 UT) with the MDI line-of-sight magnetogram closest in time (2003 June 12 01:34:59 UT), manually adjusting the alignment between the facular brightening and the weak network fields after differential rotation is taken into account. The co-alignment shows that the *TRACE* pointing should be offset by $-4''$ in both *X*- and *Y*-directions (the top panel of Figure 1), with the estimated error of 1 MDI pixel ($\sim 2''$). Here the two approaches are in agreement with each other. In the 2004 November 10 event, the Metcalf method results in an offset of $-0''.9$ and $2''.0$ in the *X*- and *Y*-directions, respectively. Again, in agreement with the Aulanier method which gives an offset of $-1''$ and $2''$ (the bottom panel of Figure 1). The 2002 May 27 event is a limb event, and only *TRACE* 195 Å images are available during the time interval of interest, thus the only method available for correcting the *TRACE* pointing is to cross-correlate one *TRACE* 195 Å image with a nearly simultaneous EUV Imaging Telescope (EIT) 195 Å image, assuming that the pointing information of the EIT full disk observations is correct. The cross-correlation (again using the routine trace_mdi_align but with the EIT keyword being invoked) shows that the *TRACE* pointing should be offset by $-4''.8$ in the *X*-direction and $-1''.6$ in the *Y*-direction (Figure 2).

2.2. 2002 May 27 Event

The failed eruption of the kinking filament on 2002 May 27 has been studied in detail by Ji et al. (2003) and Alexander et al. (2006). Ji et al. (2003) reported EUV brightening sheaths aligned along the filament legs during the kink evolution (Figure 3). Alexander et al. (2006) identified an HXR coronal emission that occurs beneath the apex of the filament close to the crossing point of the kink during the erupting phase (Figure 3(d), indicated by a white arrow). Utilizing the He I 10830 Å velocity data from Mauna Loa Solar Observatory, Alexander et al. (2006) also identified a unique "unkinking" motion of the

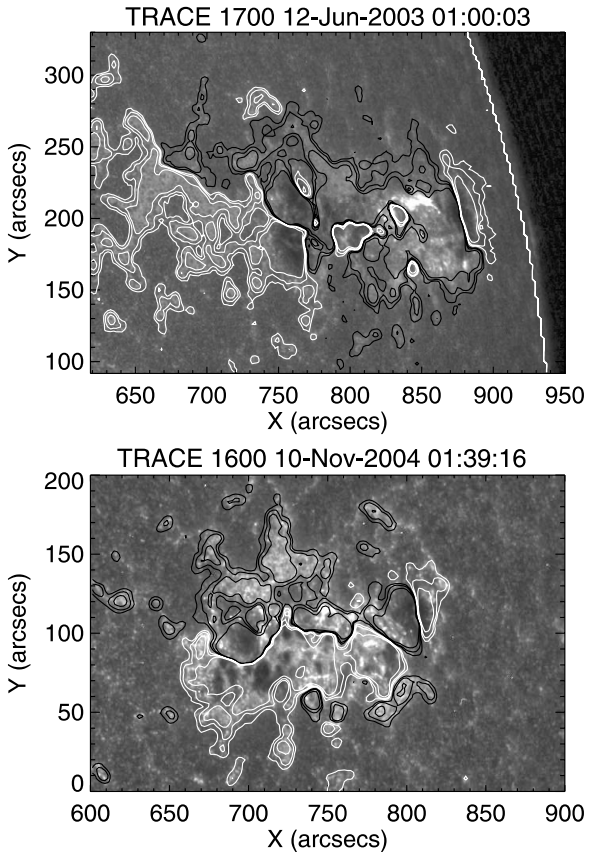

Figure 1. *TRACE* pointing correction conducted for the 2003 June 12 (top) and 2004 November 10 (bottom) events. *TRACE* images are overlaid by corresponding *SOHO* MDI magnetogram contours at 50, 100, and 200 G for positive polarities (black), and −200, −100, and −50 G for negative polarities (white). *SOHO*'s L1 view is converted to the Earth perspective, using the routine developed by T. Metcalf, mk_soho_map_earth, in the Solar SoftWare (SSW). In the 2003 June 12 event (left column), *TRACE* pointing is offset by −4″ in both *X*- and *Y*-directions. In the 2004 November 10 event (right column), *TRACE* pointing is offset by −1″ in the *X*-direction and 2″ in the *Y*-direction.

filament following the writhing motion (see Figure 4, Alexander et al. 2006). In Figure 3(b), despite two well separated footpoint sources, located at the endpoints of the filament, one can also see HXR coronal emission (marked by white arrows), which is apparently cospatial with the EUV brightening sheaths (also see Figure 3(c)). Figures 3(a)–(d) display a transition from a pair of well separated conjugate HXR footpoint sources at the endpoints of the filament, to a ribbon-like footpoint emission oriented along the endpoints of the ascending and writhing filament.

2.2.1. Imaging Spectroscopy

Imaging spectroscopic analysis is conducted for two time intervals, from 18:04:52 to 18:05:48 UT, and from 18:06:44 to 18:07:40 UT. During the first time interval, the HXR emission features coronal emission associated with the EUV brightening sheaths along the filament legs, and a pair of well separated conjugate footpoints (Figure 3(b)). During the second time interval, the HXR emission exhibits a coronal source near the crossing point of the kink and a ribbon-like footpoint emission (Figure 3(d)). We make a series of Pixon images at various energies, from which spatially resolved spectra of the coronal and the footpoint emission can then be extracted and analyzed with the Object Spectral Executive (OSPEX) package. In both time intervals, the spectrum of the coronal emission is fitted

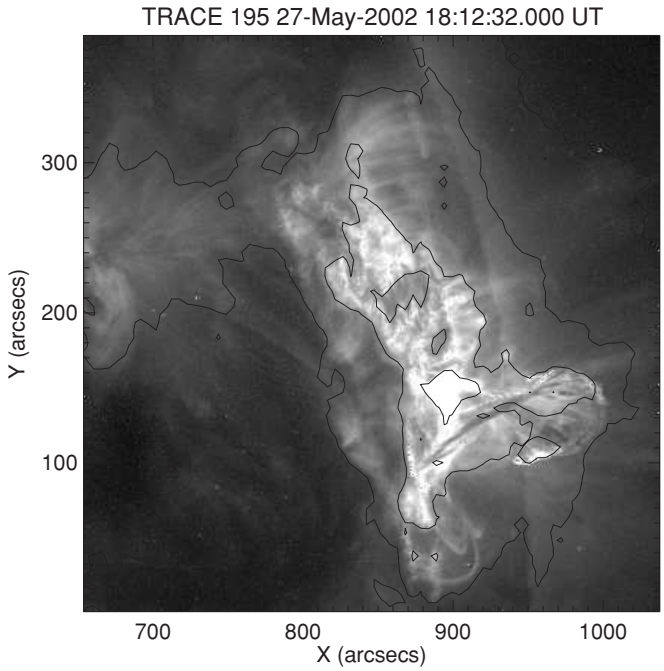

Figure 2. *TRACE* pointing correction conducted for the 2002 May 27 event. The *TRACE* 195 Å image at 18:12:32 UT is overlaid by the corresponding *SOHO* EIT 195 Å image at 18:12:11 UT. The *TRACE* pointing is offset by −4.″8 in the *X*-direction and −1.″6 in the *Y*-direction.

with an isothermal function, while the spectrum of the footpoint emission is fitted with a broken power law function, with $\gamma_1 < \gamma_2$, where γ_1 is the spectral index below the break energy and γ_2 the spectral index above the break energy.

2.3. 2003 June 12 Event

2.3.1. Kinematics

The 2003 June 12 event features twin kinking filaments (Figure 5) that originate from the same neutral line in the same active region. Both filaments activated at times within about 10 minutes apart from each other, evolved in a similar fashion, and eventually erupted together. The first kinking filament, labeled "F1" in Figure 5(e), started to rise slowly at about 01:01 UT, in the radial direction as indicated by the fiducial line. By 01:07 UT, it developed an inverse γ-shape (Figure 5(a)), and then quickly twisted into a kinked structure with two filament legs crossing each other (Figure 5(b)). The kink was fully developed at about 01:11 UT, and then remained relatively static at approximately the same height, with mass draining and probably cooling. Around 01:13 UT the second kinking filament, labeled "F2" in Figure 5(m), started to rise in a direction tilting northward from the radial, as indicated by the northwestward fiducial line. F2 followed a similar evolution pattern as F1: it first developed an inverse γ-shape at 01:14 UT, and then twisted into a kinked structure at 01:17 UT. At 01:18:39 UT, F1 started to rise again in a direction tilting southward from the radial, as indicated by the horizontal fiducial line in Figure 5(m). F2 disappeared in *TRACE* at about 01:24 UT due to decreasing contrast, but F1 can be observed to reach the western boundary of the *TRACE* FOV at 01:25:53 UT, with the assistance of running difference images (see Figure 5 and the ancillary animation), and disappeared eventually at about 01:27 UT, presumably due to filament mass ejecting out of the FOV into the high corona.

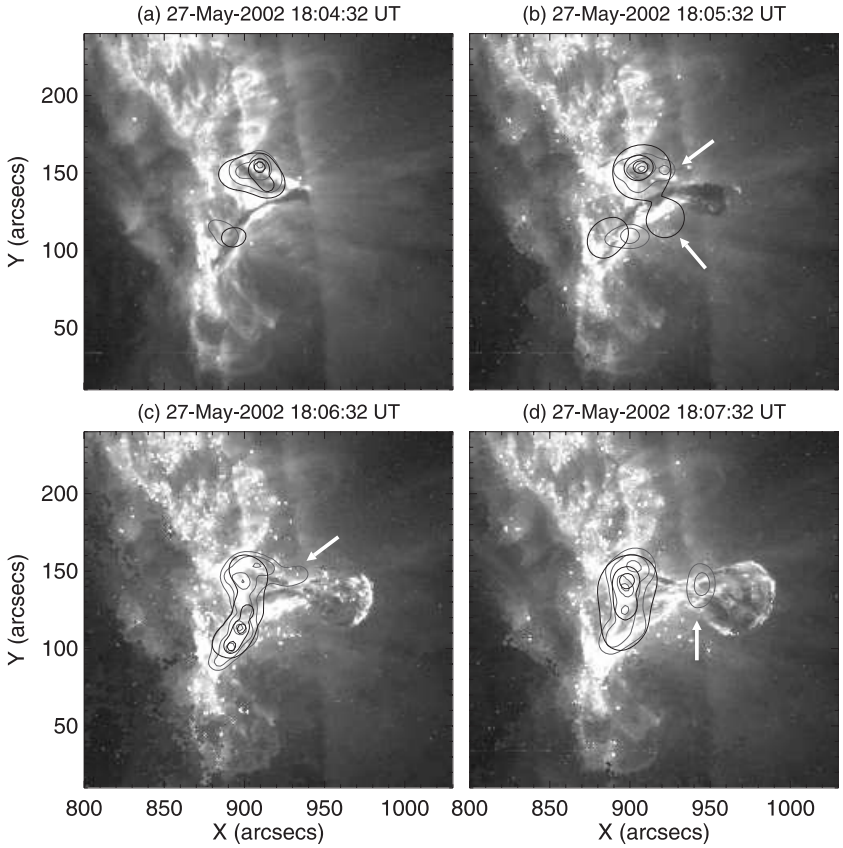

Figure 3. *TRACE* 195 Å images on 2002 May 27 overlaid with *RHESSI* X-ray contours at 10%, 20%, 50%, and 80% of the peak intensity at 12–20 keV (gray), and 20–40 keV (black). Coronal sources are marked by white arrows. The integration time for each *RHESSI* image is 12 s around the time of the corresponding *TRACE* image.

The projected displacements of both filaments are obtained by measuring the top of the filament along the fiducials as shown in Figures 5(e) and (m). All projected displacements (in arcsecs) are relative to the individual starting point (the first measurement), intending to obtain the overall shape of the profiles only. F1 experienced a three-stage evolution, namely, an initial acceleration stage, a linear stage with low speed, and a linear stage with high speed. During 01:06:12–01:09:00 UT the displacement profile of F1 is best fitted by a cubic polynomial function, $h = a + bt + ct^2 + dt^3$, with $\chi_\nu^2 = 1.02$[2] and the jerk value $d^3h/dt^3 = -9.69$ m s^{-3} (the top panel of Figure 6). From 01:09:06 UT to 01:14:15 UT, the profile is best fitted by a linear function ($\chi_\nu^2 = 0.82$), with the speed of the filament $v = 26$ km s^{-1}. From 01:14:15 UT to 01:18:35 UT, F1 was relatively static, but the draining and cooling of filament material resulted in decreasing contrast, especially for the top part of the kink structure, which makes the measurement of the exact evolution impossible. From 01:18:35 UT to 01:26:24 UT, F1 was reactivated by the eruption of F2. The displacement profile can be fitted by a linear function ($\chi_\nu^2 = 0.88$), with the speed of the filament $v = 92$ km s^{-1}, although in the later stage of the evolution, the profile shows signs of deceleration. As for F2, the displacement profile is best fitted by a cubic polynomial function ($\chi_\nu^2 = 0.26$), similar to the initial acceleration stage of F1, only with a positive jerk value 0.45 m s^{-3} (the top panel of Figure 6).

[2] χ_ν^2 is the standard deviation of the residuals, defined as χ^2/N, where χ^2 is the χ^2 estimator and N is the number of the degrees of freedom.

2.3.2. RHESSI *Imaging*

The event was accompanied by a *GOES* class M7.4 flare. From 01:07 UT to 01:26 UT, during which the twin kinking filament writhed and erupted, the *RHESSI* light curve, shown here only from the end of the *RHESSI* night at 01:10:56 UT to 01:21:00 UT, 4 s before the thick attenuator sets in, featured two major bursts in the 25–50 keV energy range (Figure 6(e)). The specific time instants when the twin kinking filaments began to develop a clear kinked structure, i.e., the two filament legs crossed each other, are marked by two arrows at the bottom of Figure 6(a). One can see that the acceleration stage of F1 is coincident with the preheating phase of the flare, during which the soft X-ray (SXR) flux increases prior to the impulsive HXR emission, as indicated by the *GOES* light curves. The eruption of F2 coincides with the first major burst in the HXR light curve, and the reactivation of F1 is apparently associated with the second major burst.

HXR sources are reconstructed from 01:11:40 UT till 01:21:00 UT. The time range is divided into consecutive 40 s intervals, during which only the thin attenuators were in front of the detectors (A1 state). An elongated HXR coronal source was observed to be aligned along the foreground leg of the kinking filament, F1, in the east–west direction, evidently deviating from the orientation of the UV flare ribbons running in the northeast–southwest direction (Figure 7). A compact footpoint emission was observed to be located at the endpoint of the same filament leg (Figures 7(b)–(f)). The coronal source appeared as early as 01:12 UT (Figure 7(a)), even before the footpoint emission was visible. As the second kinking filament, F2, rose and

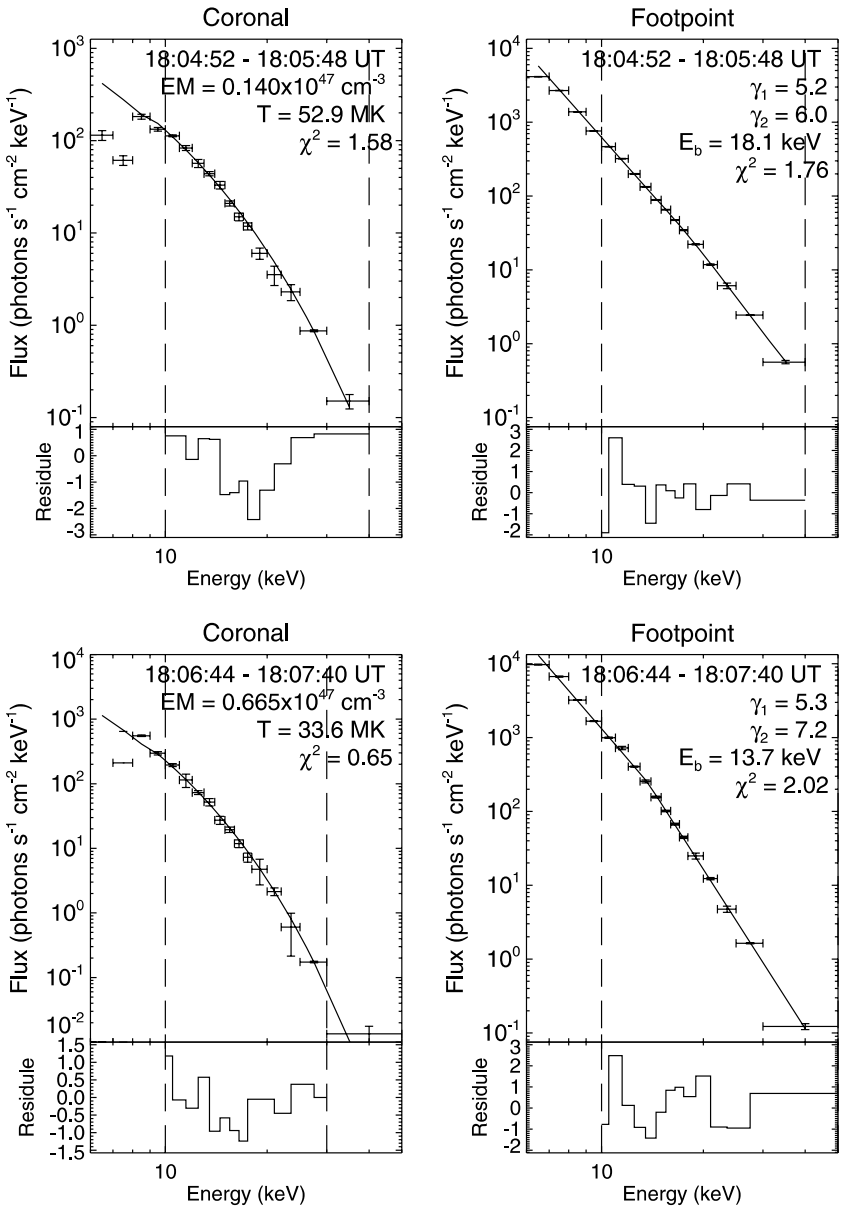

Figure 4. Imaging spectroscopy for two time intervals, from 18:04:52 to 18:05:48 UT (top), and from 18:06:44 to 18:07:40 UT (bottom). The spatially resolved spectra of both the coronal (left column) and the footpoint (right column) emission are shown with the error bars, with the horizontal error bars indicating the energy bins being used. Also shown are the broken power law as well as the thermal fits in solid lines, and the corresponding normalized residuals at the bottom of each panel.

kinked, the elongated coronal source was still aligned along the foreground leg of the kinking filament F1 (Figures 7(d) and (e)), despite the westward motion of F1. There seems to be a second coronal source associated with F2 (Figures 7(d) and (e)), but the long time integration required for the image reconstruction in this event and the limitation of the *RHESSI* spatial resolution prevent us to pinpoint its temporal and spatial relationship with the evolution of F2. One can see that the twin kinking filaments appear to share the same footpoint emission, which implies that this region is the source of the destabilization of both eruptions.

2.3.3. Imaging Spectroscopy

Imaging spectroscopy is conducted separately for the two bursts in the 25–50 keV light curve during the early impulsive phase of the flare, which covers a 1 minute time interval from 01:12:32 to 11:13:32 UT, and a 52 s time interval from 01:17:40 to 01:18:32 UT (the dotted lines in Figure 6(e)). For both time intervals, the spectrum of the coronal source can be fitted with an isothermal function with a temperature of 20–30 MK; and the spectrum of the footpoint source can be fitted with a broken power-law function with $\gamma_2 \approx \gamma_1 + 2$ and the break energy $E_b \approx$12–14 keV (Figure 8).

2.4. 2004 November 10 Event

The 2004 November 10 event has been studied in detail by Williams et al. (2005). Prior to the filament eruption, four precursor ribbons are observed in *TRACE* UV continuum (1600 Å), suggestive of the quadrupolar nature of the active region. During the eruption, the eruptive filament rose as a kinked structure with an exponential growth of height within the *TRACE* FOV. The dynamic evolution of the kinking filament

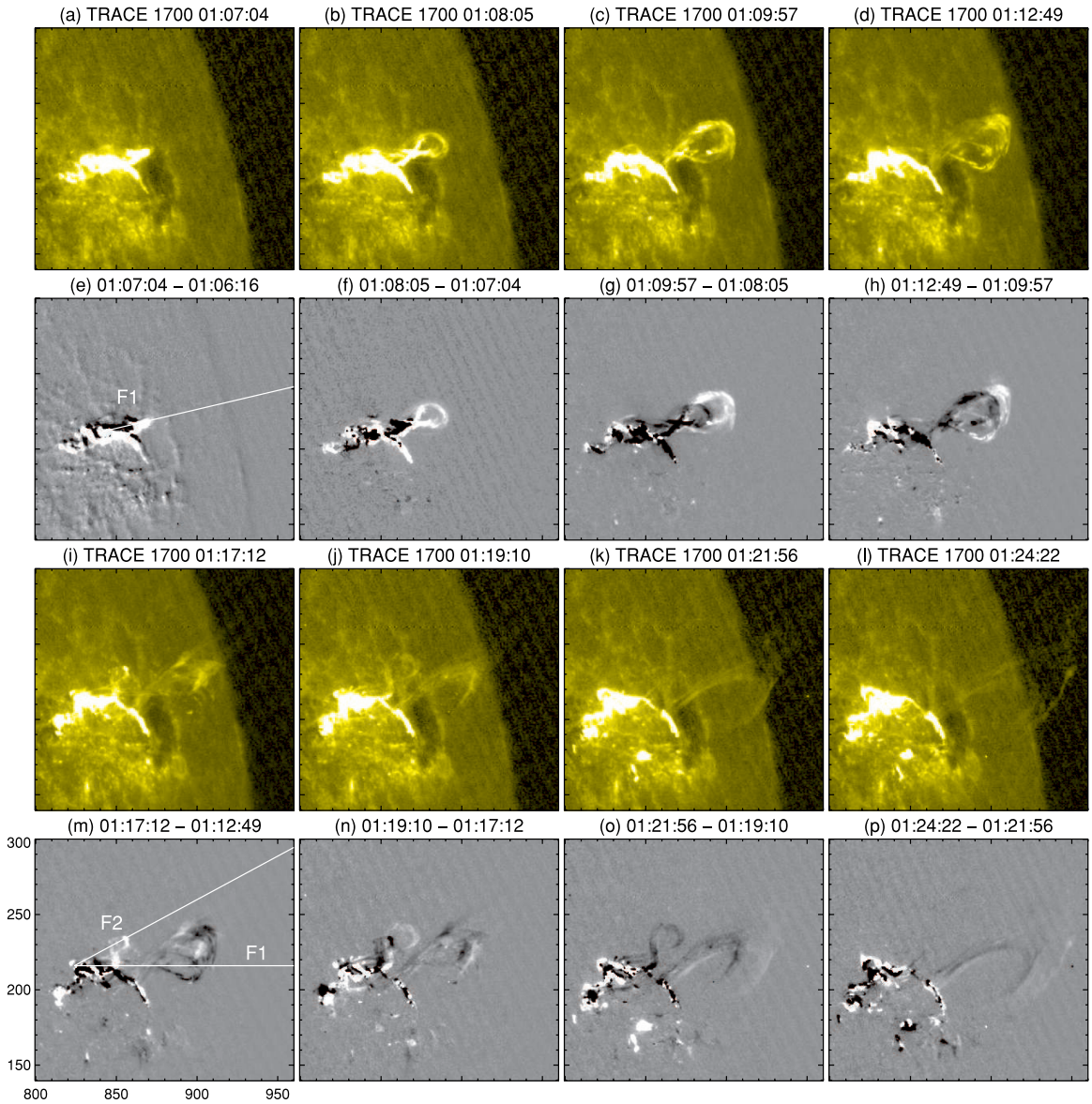

Figure 5. *TRACE* 1700 Å images and the corresponding running difference images showing the eruption of the twin kinking filaments on 2003 June 12. Images are all normalized to DN/s. The twin kinking filaments are labeled as "F1" and "F2," respectively. Fiducials in (e) and (m) show the directions along which the filaments erupted.

(A color version and an avi animation of this figure are available in the online journal.)

is in qualitative agreement with MHD numerical simulations of a kink-unstable magnetic flux rope. Williams et al. (2005) therefore concluded that the MHD helical kink instability is most likely the driver of the eruption while tether weakening by breakout-like quadrupolar reconnection may be the release mechanism.

2.4.1. RHESSI *Imaging*

The event was associated with a *GOES* class X2.5 flare. HXR emission features in this event were well observed by *RHESSI*. We concentrate on the early impulsive phase of the flare, from 02:01:48 to 02:06:12 UT, during which only the thin attenuator was in front of the detectors (A1 state). At 02:06:16 UT, the thick attenuator also moved in (A3 state). HXR count rates at lower energies (below 30 keV) increased gradually as early as 02:01:48 UT, while the count rates of more energetic photons only began to increase from 02:03:48 UT onward.

Figures 9(a)–(i) were overlaid with *RHESSI* contours in three energy bands, namely, 6–12 keV (red), 12–30 keV (green), and 30–80 keV (blue). One can see that there were two concurrent but separate flare emissions taking place during the early impulsive phase of the flare, labeled "E1" and "E2" in Figure 9(a). In the corresponding *Solar and Heliospheric Observatory* (*SOHO*) MDI line-of-sight magnetogram (Figure 9(j)) overlaid with the same *RHESSI* contours as in Figure 9(a), one can see that E1 occurred at the neutral line, "L1," which separates small patches of negative flux from the dominant positive flux in the center of the active region. E2 is associated with the neutral line, "L2," which separates the leading sunspot of positive flux from small patches of negative flux located to the northwest of the leading sunspot.

The filament was oriented predominantly in the east–west direction. It began to rise slowly as early as about 02:02:00 UT and exhibited an inverse γ-configuration at about 02:03:30 UT (Figures 9(a) and (b)). From 02:04:14 UT onward (the time

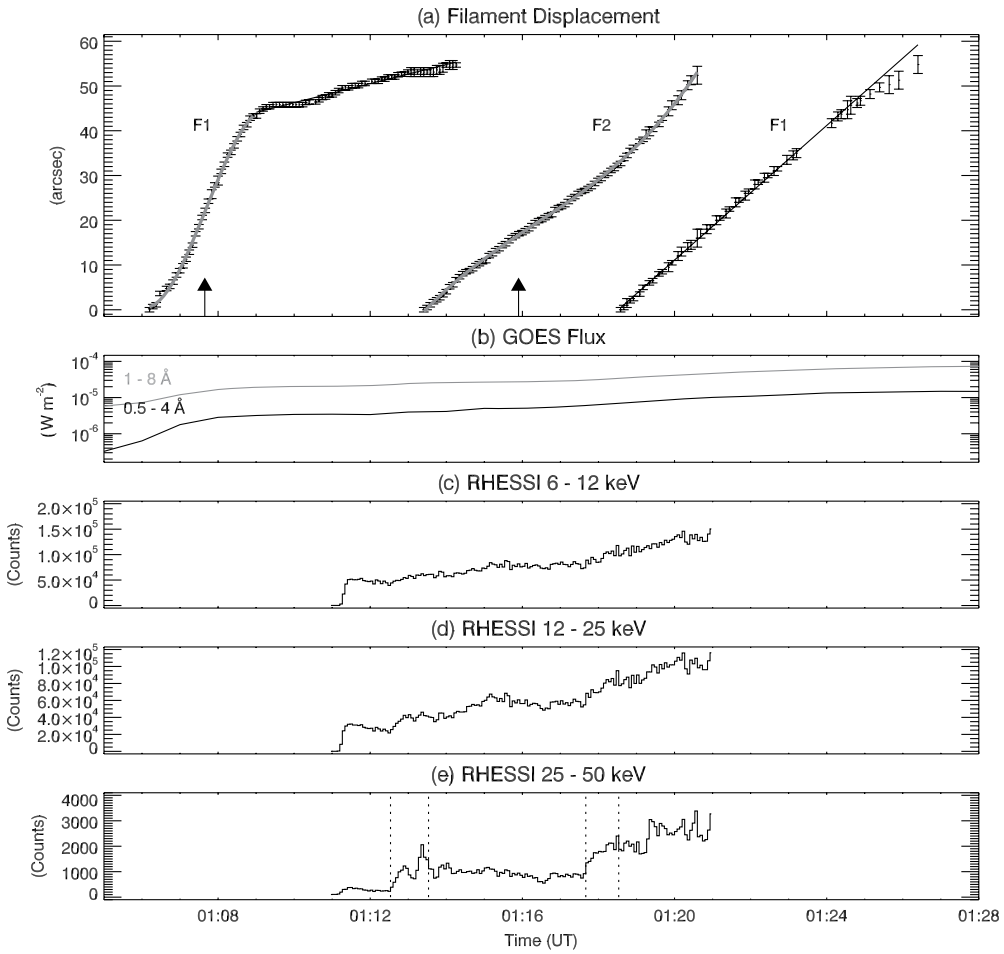

Figure 6. Kinematic evolution of the twin kinking filaments and the associated X-ray fluxes recorded by *RHESSI* and *GOES* during the early impulsive phase of the flare on 2003 June 12. (a) Projected displacements of the twin kinking filaments, fit with a cubic polynomial function (thick gray line), or a linear function (thin black line). The first (second) arrow at the bottom indicates the time when the first (second) filament began to display a clear kinking signature, with two legs crossing each other at 01:07:39 (01:15:54) UT. (b) *GOES* soft X-ray flux in two bands, 1–8 Å and 0.5–4 Å. (c)–(e) *RHESSI* counts at a 4 s resolution in the 6–12, 12–25 and 25–50 keV energy bands, respectively. The dotted lines indicate two time intervals that are used to conduct imaging spectroscopy analysis.

instant is marked by an arrow at the bottom of Figure 9(k)), the filament displayed a clear kinked structure with two filament legs crossing each other (Figures 9(c)–(i)). As soon as the filament was fully kinked, a coronal source in the 12–30 keV energy range was observed to be located in the neighborhood of the projected crossing point of the kink, and to rise slowly with the kinking filament. The coronal source disappeared after the kinking filament began to ascend and expand upward eruptively at about 02:06 UT (Figure 9(i)). The filament erupted out of the *TRACE* FOV at 02:06:48 UT. Meanwhile, E1 initially featured relatively compact footpoint emission close to the endpoints of the filament (Figures 9(a)–(e)). As the eruption progressed, E1 exhibited multiple footpoint sources extended along the UV flare ribbons beneath the kinking filament (Figures 9(f)–(i)), suggestive of a similar morphological transition as observed in the 2002 May 27 event.

2.4.2. Imaging Spectroscopy

Spatially resolved spectra for both the footpoint and the coronal sources are obtained for a 1 minute interval (bounded by dotted lines in Figure 9(k)), from 02:04:44 UT to 02:05:44 UT, when the observed coronal source is well separated from both HXR emissions E1 (southern footpoints) and E2 (northern footpoints). All three spectra are fitted with a broken power-law function (Figure 10). However, the spectra of both the coronal source and the HXR emission E1 are harder than that of E2 and that the break energy of E1 is also significantly higher than that of E2, which is in line with our interpretation that E1 and E2 are separate HXR emissions, and that E1 is more closely associated with the coronal emission.

3. DISCUSSION AND CONCLUSION

3.1. Interpretation of Observations

Figure 11 summarizes our understanding of how the dynamic evolution of kinking filaments impacts on the HXR emission. In this cartoon, the filament is represented by a thick solid line, the overlying potential-like field by a single thin loop (but bear in mind that there are a whole arcade of loops), and the magnetic neutral line by a dashed line. The explosion-like shapes indicate the sites of magnetic reconnection in the corona, and the circular or elliptical shapes represent the consequent EUV or X-ray emission.

As the filament field is mainly directed along the filament spine (Tandberg-Hanssen 1995, Section 3.5), the field in the two filament legs are effectively opposing each other in an archlike filament. As a consequence, reconnection may occur where the two filament legs are "squeezed" together due to the writhing

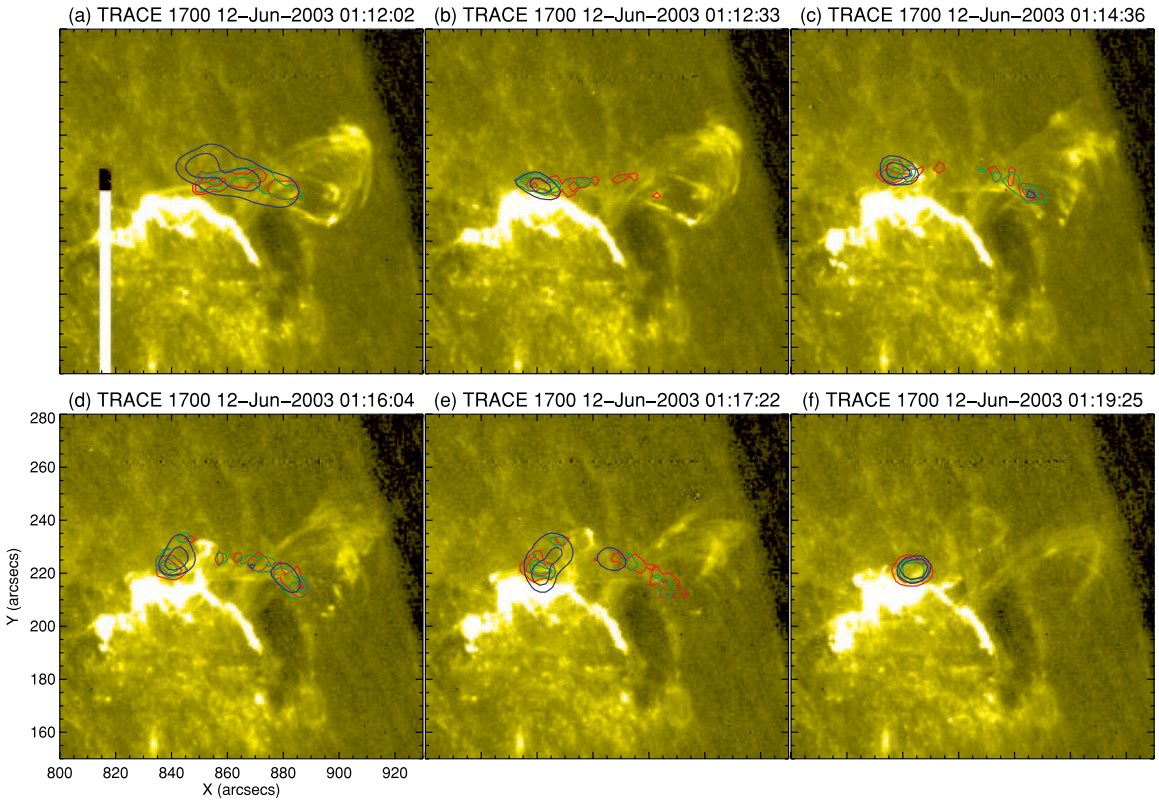

Figure 7. *TRACE* 1700 Å images overlaid with contours at 30% and 60% of the peak brightness in 6–12 (red), 12–25 (green), and 25–50 keV (blue) of each individual *RHESSI* image.

(A color version of this figure is available in the online journal.)

motion (Phase I; the top panel of Figure 11), reminiscent of the F&G simulations.

As the filament ascends and expands upward, overlying magnetic field lines are stretched and pinched, yielding a current sheet underneath the filament, where field lines may reconnect. The reconnection takes place throughout the overlying arcade, therefore leading to ribbon-like HXR footpoint emission underneath the rising filament (see also Figures 3(c), 3(d), and 9(d)–(h)). In this scenario, the reconnection occurs at an X-type magnetic topology beneath the filament arch (Phase II; the bottom panel of Figure 11), reminiscent of the vertical current sheets generated in the T&K simulations as well as in the later stage of the F&G simulations. Both the 2002 May 27 and 2004 November 10 events show signs of a transition from Phase I to Phase II, in terms of flare morphology.

In Phase I, particles that are accelerated at the reconnection site will precipitate along the field lines, in this case, the filament legs, to the dense chromosphere where they lose most of their energy in Coulomb collisions and emit HXR bremsstrahlung, as evidenced by the compact HXR footpoint sources at the endpoints of the filament (see Figures 3(a), 3(b), 7(b)–(f), and 9(c)). The reconnection can also heat up the local plasma and cause an expansion, with thermal conduction fronts that propagate along the magnetic field direction down to the chromosphere (e.g., Priest & Forbes 2002), which can heat the plasma along the field lines (e.g., Chen et al. 1999). In both the 2002 May 27 and 2003 June 12 events, the imaging spectroscopic analysis shows that the coronal emission is very likely thermal, produced by plasma with temperatures above 20 MK. In the 2002 May 27 event, the coronal HXR emission in Phase I is associated with the *TRACE* 195 Å brightening sheaths along the filament legs (Figure 3). It is well known that the 195 Å band contains an Fe 24 line at 192 Å, emitted by plasma at 20 MK during flares (e.g., Warren et al. 1999; Tripathi et al. 2006).

Alternatively, in both phases, accelerated particles may also deposit energy in corona due to the presence of filament material, which is up to 2 orders of magnitude denser than the surrounding coronal plasma, i.e., 10^{10} cm^{-3} $< n_e <$ 10^{11} cm^{-3} (Tandberg-Hanssen 1995, Section 3.3). In the 2003 June 12 event, the coronal source even appeared before the footpoint emission was observed (Figure 7(a)). This is reminiscent of the observation reported by Veronig & Brown (2004) who suggested a very high coronal density result that HXR emission is dominantly seen in the corona rather than in the chromosphere. Models constrained by observed emission line profiles, however, suggest that a filament is an ensemble of small threads, with the value of the filling factor between 0.01 and 0.1 (e.g., 1995, Section 5.3; Wiik et al. 1999). Thus, only part of the accelerated particles can be stopped even in the filament body. The collisional heating of the coronal region results in HXR as well as SXR emission, while the rest of the accelerated particles are still able to generate the observed footpoint emission. This may be the case in the 2004 November 10 event. During the time interval when the coronal emission was observed, the spectrum of the E1 emission (southern footpoints), which is more closely associated with the coronal emission than the E2 emission (northern footpoints), is well fitted by a broken power law function with the break energy of about 30 keV, while the coronal emission is preferentially observed at 12–30 keV, whose spectrum is also well fitted with a broken power law function with $\gamma_2 - \gamma_1 = 1.6$. This is in approximate agreement with the

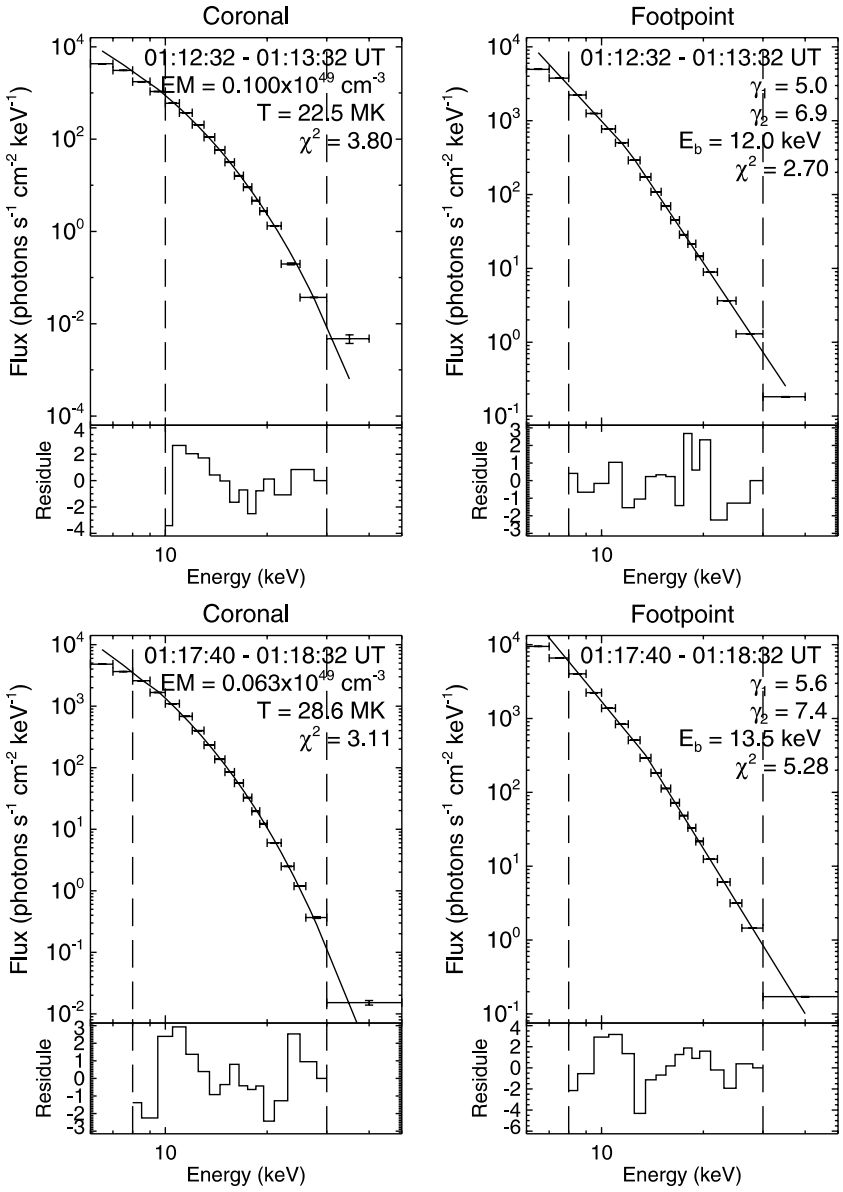

Figure 8. Imaging spectroscopy results for two time intervals, from 01:12:32 to 11:13:32 UT (top), and from 01:17:40 to 01:18:32 UT (bottom). The spatially resolved spectra of both the coronal (left column) and the footpoint (right column) emission are shown with the error bars, with the horizontal error bars indicating the energy bins being used. Also shown are the broken power law as well as the thermal fits in solid lines, and the corresponding normalized residuals at the bottom of each panel.

thick–thin target model (e.g., Metcalf & Alexander 1999), which suggests that the dense coronal region responsible for the coronal HXR emission acts as thick target for lower energetic electrons, and thin target for higher energies, therefore predicting $\gamma_2 - \gamma_1 = 2$.

However, we should put more emphasis on the morphology of the footpoint emission in distinguishing the two phases, due to the two caveats below.

1. The coronal source is normally much fainter than the corresponding footpoint emission, which makes the reconstruction of the coronal source less reliable due to poorer photon statistics.
2. *RHESSI* spatial resolution is relatively poor compared to the 1″ resolution of *TRACE* data: the FWHM of the finest grid (detector 3) we used to reconstruct HXR sources is 6.″79, comparable to the "width" of the filament spine. Thus, for the relatively small kink as observed in the later two events, it is less likely that we are able to distinguish the elongated coronal HXR emission orientated along two filament legs in Phase I from the coronal emission near the crossing point of the kink in Phase II.

3.2. Conclusion

In conclusion, HXR emission with distinct morphological features are identified in a two-phase kink evolution of eruptive filaments. Phase I features compact footpoint sources at the endpoints of the filament and coronal emission along the legs of the kinking filament. It occurs as a result of the interactions of the two filament legs undertaking writhing motions. Phase II features a ribbon-like footpoint emission extending along the endpoints of the filament and a coronal emission near the crossing point of the kink. In the later scenario, due to the rise and expansion of the filament, an arcade of overlying field lines are brought together below the apex of the filament, where an

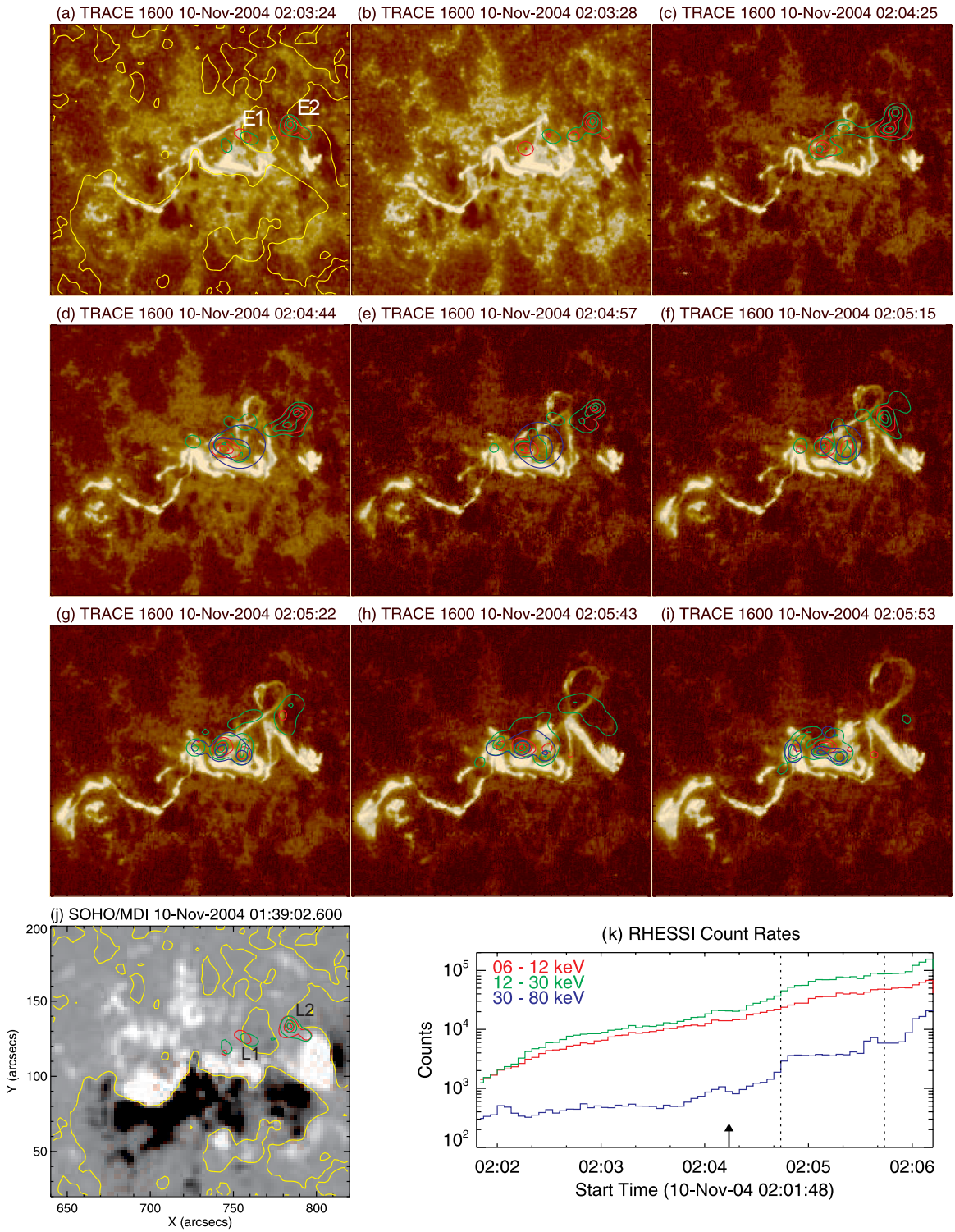

Figure 9. X2.5 flare on 2004 November 10 observed in UV continuum and X-rays. (a)–(i) *TRACE* 1600 Å images overlaid with *RHESSI* contours at 20%, 50%, and 80% of the peak brightness at 6–12 keV (red) and 12–30 keV (green), and contours at 30% and 60% at 30–80 keV (blue). Two separate flare emissions are labeled E1 and E2 in (a), which is overlaid with the neutral lines (yellow) computed from the photospheric magnetogram in panel (j). (j) A *SOHO* MDI magnetogram taken at 01:39:02 UT is differentially rotated to 02:03:24 UT, overlaid with the same contours as in (a). The neutral lines that are associated with the HXR emission E1 and E2 are labeled L1 and L2, respectively. (k) *RHESSI* counts at 4 s resolution in three energy bands. The arrow indicates the time when a clear kinked structure was first observed. The dotted lines indicate the time interval for the imaging spectroscopic analysis.

(A color version of this figure is available in the online journal.)

X-type current sheet forms. Owing to the symmetry of this configuration, magnetic reconnection occurs preferentially at the half height of the filament, coincident with the crossing point of the kink in the two-dimensional projection, as illustrated in Figure 11. The evolution of the HXR emission in both the 2002 May 27 and 2004 November 10 events exhibits a transition from Phase I to Phase II, while the 2003 June 12 event mostly features Phase I emission.

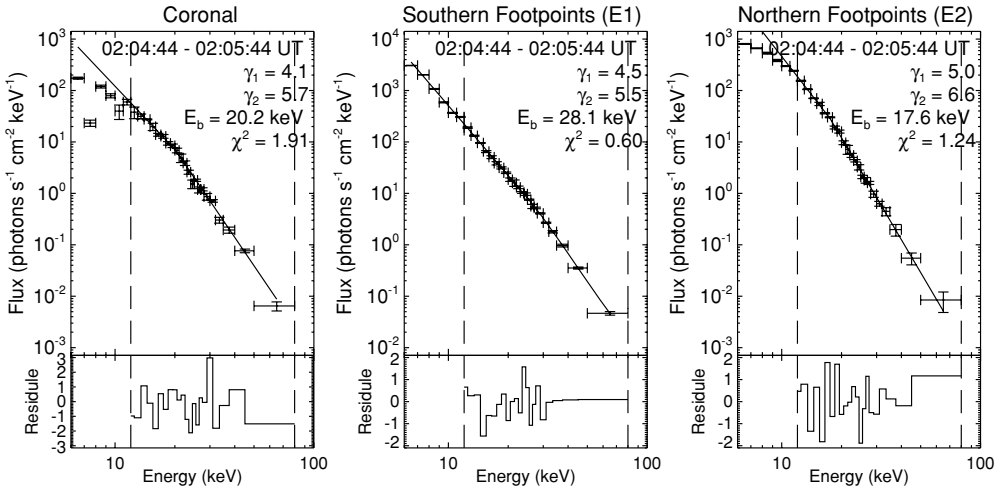

Figure 10. Imaging spectroscopy result for the time interval from 02:04:44 UT to 02:05:44 UT on 2004 November 10. The spatially resolved spectra of individual HXR sources are shown with the error bars, with the horizontal error bars indicating the energy bins being used. Also shown are the broken power law fits in solid lines, and the corresponding normalized residuals at the bottom of each panel.

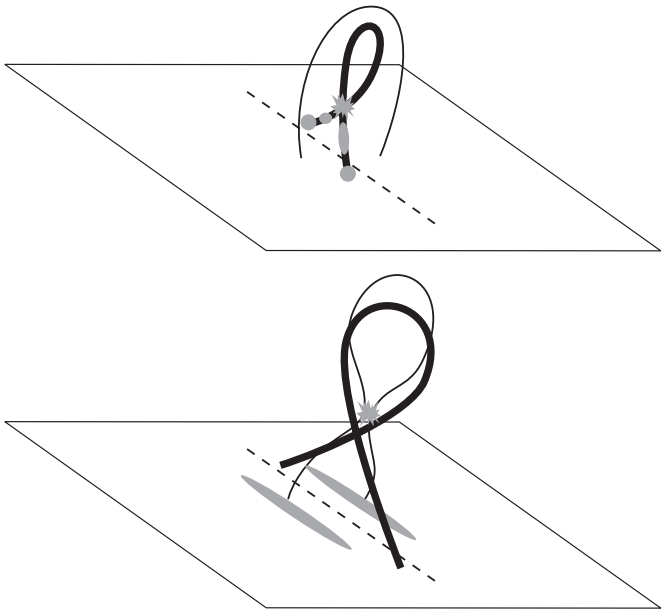

Figure 11. Cartoon showing the reconnection and HXR emission in a kinking filament. The filament is represented by a thick loop, the overlying field by a thin loop (but bear in mind that there are a whole arcade of loops), and the magnetic neutral line by a dashed line. The explosion-like shapes indicate reconnections in the corona. The grey circular or elliptical shapes indicate EUV or X-ray emissions. Top: Phase I of the evolution (see the text). Bottom: Phase II of the evolution (see the text).

The authors thank the *TRACE* and *RHESSI* consortia for the excellent data. This work was supported by NASA grant NNG04GO68G.

REFERENCES

Alexander, D., & Coyner, A. J. 2006, ApJ, 640, 505
Alexander, D., Liu, R., & Gilbert, H. R. 2006, ApJ, 653, 719
Alexander, D., & Metcalf, T. R. 1997, ApJ, 489, 442
Amari, T., & Luciani, J. F. 1999, ApJ, 515, L81
Amari, T., Luciani, J. F., Aly, J. J., & Tagger, M. 1996, ApJ, 466, L39
Aschwanden, M. J., et al. 2004, Sol. Phys., 219, 149
Aulanier, G., DeLuca, E. E., Antiochos, S. K., McMullen, R. A., & Golub, L. 2000, ApJ, 540, 1126
Aulanier, G., Démoulin, P., & Grappin, R. 2005, A&A, 430, 1067
Baty, H. 2000, A&A, 360, 345
Baty, H., & Heyvaerts, J. 1996, A&A, 308, 935
Berger, M. A. 1984, Geophys. Astrophys. Fluid. Dyn., 30, 79
Chen, P. F., Fang, C., Tang, Y. H., & Ding, M. D. 1999, ApJ, 513, 516
Fan, Y. 2005, ApJ, 630, 543
Fan, Y., & Gibson, S. E. 2003, ApJ, 589, L105
Fan, Y., & Gibson, S. E. 2004, ApJ, 609, 1123
Gerrard, C. L., Arber, T. D., Hood, A. W., & Van der Linden, R. A. M. 2001, A&A, 373, 1089
Gerrard, C. L., & Hood, A. W. 2003, Sol. Phys., 214, 151
Gerrard, C. L., Hood, A. W., & Brown, D. S. 2004, Sol. Phys., 222, 79
Gibson, S. E., & Fan, Y. 2006, ApJ, 637, L65
Gibson, S. E., Fan, Y., Mandrini, C., Fisher, G., & Demoulin, P. 2004, ApJ, 617, 600
Gibson, S. E., Fan, Y., Török, T., & Kliem, B. 2006, Space Sci. Rev., 124, 131
Green, L. M., Kliem, B., Török, T., van Driel-Gesztelyi, L., & Attrill, G. D. R. 2007, Sol. Phys., 246, 365
Hood, A. W. 1992, Plasma Phys. Contr. F., 34, 411
Hood, A. W., & Priest, E. R. 1979, Sol. Phys., 64, 303
Hurford, G. J., et al. 2002, Sol. Phys., 210, 61
Ji, H., Wang, H., Schmahl, E. J., Moon, Y.-J., & Jiang, Y. 2003, ApJ, 595, L135
Kliem, B., Titov, V. S., & Török, T. 2004, A&A, 413, L23
Klimchuk, J. A., Antiochos, S. K., & Norton, D. 2000, ApJ, 542, 504
Lionello, R., Velli, M., Einaudi, G., & Mikic, Z. 1998, ApJ, 494, 840
Liu, R., Alexander, D., & Gilbert, H. R. 2007, ApJ, 661, 1260
Liu, R., Gilbert, H. R., Alexander, D., & Su, Y. 2008, ApJ, 680, 1508
Low, B. C., & Berger, M. A. 2003, ApJ, 589, 644
Metcalf, T. R., & Alexander, D. 1999, ApJ, 522, 1108
Metcalf, T. R., Alexander, D., Hudson, H. S., & Longcope, D. W. 2003, ApJ, 595, 483
Metcalf, T. R., et al. 1996, ApJ, 466, 585
Priest, E. R., & Forbes, T. G. 2002, A&AR, 10, 313
Roussev, I. I., et al. 2003, ApJ, 588, L45
Rust, D. M., & LaBonte, B. J. 2005, ApJ, 622, L69
Seehafer, N. 1986, Sol. Phys., 105, 223
Tandberg-Hanssen, E. 1995, The Nature of Solar Prominences (Dordrecht: Kluwer)
Titov, V. S., & Démoulin, P. 1999, A&A, 351, 707
Titov, V. S., Galsgaard, K., & Neukirch, T. 2003, ApJ, 582, 1172
Titov, V. S., Hornig, G., & Démoulin, P. 2002, J. Geophys. Res., 107, 1164
Titov, V. S., Priest, E. R., & Demoulin, P. 1993, A&A, 276, 564
Török, T., & Kliem, B. 2003, A&A, 406, 1043
Török, T., & Kliem, B. 2005, ApJ, 630, L97
Török, T., Kliem, B., & Titov, V. S. 2004, A&A, 413, L27
Tripathi, D., Del Zanna, G., Mason, H. E., & Chifor, C. 2006, A&A, 460, L53
van Hoven, G., Mok, Y., & Mikic, Z. 1995, ApJ, 440, L105
Veronig, A. M., & Brown, J. C. 2004, ApJ, 603, L117
Warren, H. P., et al. 1999, ApJ, 527, L121
Wiik, J. E., Dammasch, I. E., Schmieder, B., & Wilhelm, K. 1999, Sol. Phys., 187, 405
Williams, D. R., Török, T., Démoulin, P., van Driel-Gesztelyi, L., & Kliem, B. 2005, ApJ, 628, L163